

Corrosion of UNS G10180 Steel in Supercritical and Subcritical CO₂ with O₂ as a Contaminant

Nor Roslina Rosli,
Institute for Corrosion and Multiphase
Technology,
342 West State Street, Athens, OH 45701

Srdjan Nestic,
Institute for Corrosion and Multiphase
Technology,
342 West State Street, Athens, OH 45701

Yoon-Seok Choi
Institute for Corrosion and Multiphase
Technology,
342 West State Street, Athens, OH 45701

David Young
Institute for Corrosion and Multiphase
Technology,
342 West State Street, Athens, OH 45701

ABSTRACT

This paper reports the corrosion behavior of mild steel in supercritical CO₂ with O₂ as a contaminant. The contaminant concentration corresponds to the amount of O₂ that can be present in CO₂ from an oxyfuel combustion flue gas. The effect of O₂ (4 vol. %) on the corrosion performance of mild steel (UNS G10180) in CO₂-saturated brine was investigated using a 4-liter stainless steel autoclave for 48 hours. Experiments were conducted at two different temperatures (25°C and 80°C) and two different CO₂ partial pressures (4 and 9 MPa) combinations, which involve gaseous, liquid, and supercritical CO₂. Electrochemical and weight loss measurements as well as characterization of the corrosion product were conducted in this study. Experiments at 80°C revealed corrosion product bilayers on the steel surface, whereas the experiments at 25°C were essentially devoid of corrosion product layers. The bilayer consisted of iron carbonate, iron oxides, and iron oxyhydroxides. The coherence of the iron carbonate layer provided protection to the steel surface. Overall, the corrosion rates at the end of the experiments were much higher at 25°C than at 80°C. Specimens recovered from experiments conducted at 80°C exhibited localized corrosion, while the specimens from 25°C experiments displayed severe general corrosion.

INTRODUCTION

High pressure CO₂ is typically transported *via* mild steel pipelines to CO₂-EOR injection sites. The CO₂ can be derived from several sources, such as from CO₂ geologic reservoirs, coal gasification, natural gas processing, and potentially from fossil fuel-fired power plants. However, this last source of CO₂ contains impurities, such as O₂, SO_x and NO_x. Consequently, research to investigate the corrosion behavior of mild steel in supercritical and subcritical CO₂ in the presence of O₂ as a contaminant is important. The contaminant concentration should correspond to the amount of O₂ that can be present in CO₂ from, for example, an oxyfuel combustion flue gas. O₂ concentration in a CO₂ stream from oxyfuel process can be as high as 3 vol.%¹ and further purification of the gas to eliminate the O₂ is considered economically unfeasible. Previous studies have found that the existence of O₂ in sweet corrosion

systems accelerated the corrosion rate of steel²⁻⁵ at various CO₂ partial pressures and caused pitting corrosion⁶⁻⁹ in different kinds of steels. The corrosion mechanisms, especially at high CO₂ partial pressure, have not been fully investigated. In this work, the effect of O₂ (4 vol.%) on the corrosion performance of mild steel (UNS G10180) in CO₂-saturated brine was investigated using a 4-liter autoclave for 48-hour. Experiments were conducted at temperature and pressure combinations that correspond to subcritical and supercritical conditions.

EXPERIMENTAL PROCEDURES

Sample Material and Preparation

Carbon steel UNS G10180 with a ferritic/pearlitic microstructure was used in the present study to represent casing and tubing material. The test material was analyzed using Atomic Emission Spectroscopy, and the composition of the steel was confirmed to be in conformance with the standard UNS G10180 [10] with chemical content 0.18 wt.% C, 0.75 wt.% Mn, 0.001 wt.% P, 0.021 wt.% S, and the balance is Fe with other trace alloying elements. Cylindrical steel specimens were utilized for the electrochemical measurements, while flat rectangular steel specimens were utilized for weight loss and surface analysis. The specimens were polished with a 600 grit silicon carbide paper, cleaned with isopropanol in an ultrasonic bath, and dried using a heat gun prior to the test. The mass and the dimensions of the specimens were measured.

Experimental Set-up and Instrumentation

All tests in this research were conducted in a 4-liter stainless steel autoclave as illustrated in Figure 1. The setup consisted of a Pt-coated Nb counter electrode, a shaft for the steel specimen as the working electrode, Ag/AgCl reference electrode, and a glass pH electrode that were all inserted through the stainless steel lid of the autoclave. The electrodes were immersed in 3 liters of 1 wt.% NaCl solution saturated with CO₂ for at least 2 hours prior to the start of each experiment. The temperature of the vessel was controlled by a digital controller connected to the autoclave. O₂ was introduced into the sealed autoclave until the desired partial pressure was achieved. The O₂ gas input was then shut off for the entire duration of the test. High pressure CO₂ was then pumped into the autoclave until the desired total pressure was achieved. The condition of the tests was a non-refreshing closed system, therefore changes in the partial pressure of the gases was expected. The O₂ content at the end of the tests were determined by mass balance calculations.

Measurements and Test Matrix

Experiments were conducted at two different temperatures (25°C and 80°C) and two different CO₂ partial pressures, 4 MPa and 9 MPa, as shown in Table 1. All tests were compared with a baseline condition without the presence of O₂. Corrosion rates were measured continuously using the linear polarization resistance (LPR). Electrochemical impedance spectroscopy (EIS) was also conducted to determine the value of the solution resistance in order to correct the polarization resistance values obtained from LPR measurements. Besides LPR, the average corrosion rates were also determined via weight loss measurement at the end of the 48-hour tests. After completion of the high-pressure tests, the flat steel specimens were removed from the autoclave, rinsed with isopropanol, placed in individual nitrogen-purged bags, and stored in a dry cabinet. Further analyses of the specimens were conducted using scanning electron microscopy (SEM), energy dispersive x-ray spectroscopy (EDS), Raman spectroscopy, and x-ray diffraction (XRD). The surface of the steel underneath the corrosion product was analyzed by carefully removing the corrosion product using Clarke solution (ASTM G1-03)⁽¹⁾. The surface of the bare steel surface was examined using SEM, and by 3D profilometry.

⁽¹⁾ American Society for Testing and Materials (ASTM), 100 Barr Harbor Drive, PO Box C700, West Conshohocken, PA, 19428-2959

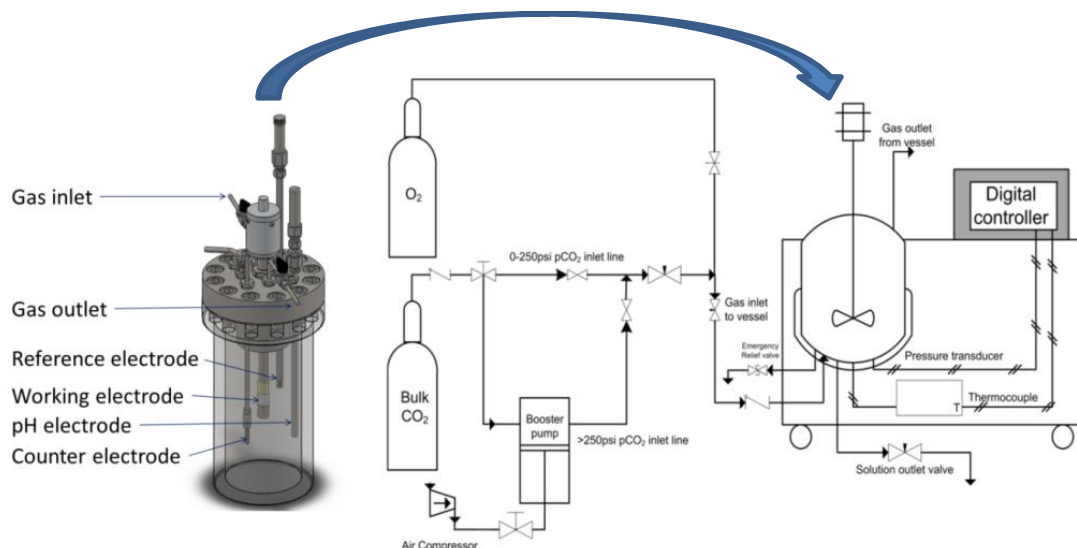


Figure 1: Schematic, and piping and instrumentation diagram of the stainless steel autoclave

**Table 1
Test Matrix**

Expt.	T (°C)	pCO ₂ (MPa)	pO ₂ (MPa)	CO ₂ phase
1	25	4	0	Gas
2	25	9	0	Liquid
3	80	4	0	Gas
4	80	9	0	Supercritical
5	25	4	0.17	Gas
6	25	9	0.375	Liquid
7	80	4	0.17	Gas
8	80	9	0.375	Supercritical

RESULTS AND DISCUSSION

Experiment 1: 25°C, 4 MPa pCO₂, with and without 4% O₂.

In this experiment, the CO₂ is in the gaseous phase. Figure 2 shows the variation of corrosion rate with time for the cases with and without O₂ at 4 MPa CO₂ and 25°C as measured by LPR. The presence of O₂ in the system showed an increase in the overall corrosion rate of the steel sample. These values were integrated with time and were comparable to the weight loss corrosion rate that was measured at the end of 48-hour experiments (Figure 3). The corrosion potential of both systems, however, did not show a significant difference between each set of experiments.

The steel sample immersed in the anoxic environment for 48 hours had an amorphous and very thin gray-colored corrosion product on its surface with obvious absence of any crystalline features as shown in Figure 4. On the other hand, the steel sample from the CO₂/O₂ experiments appeared to have a thin layer of bluish-green corrosion product that turned yellowish after about 20 to 30 minutes. Both samples from the oxic and anoxic conditions displayed similar surface morphology under SEM. The

elemental analysis using EDS indicated a higher level of oxygen, O, that expected due to the presence of a thin iron oxide layer on the steel surface. Alloying elements such as molybdenum (Mo), manganese (Mn), and copper (Cu) were also detected on the steel surface.

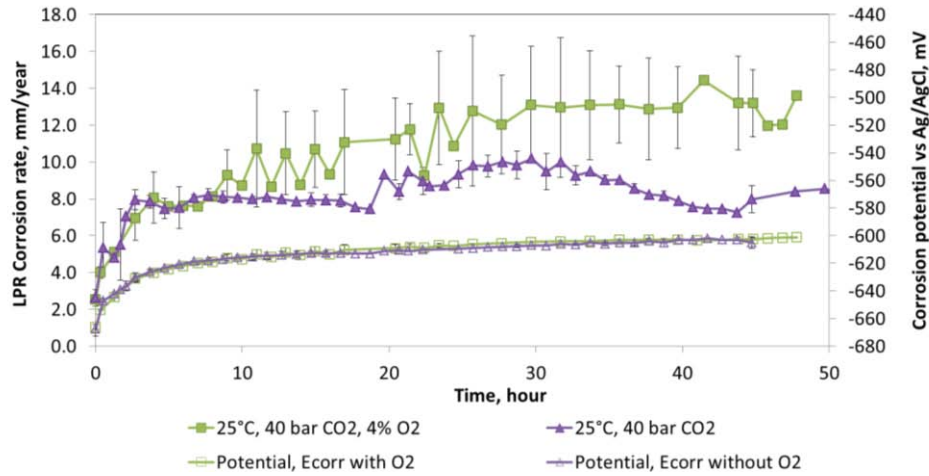


Figure 2: LPR corrosion rate and its corresponding corrosion potentials with time for experiments at 25°C, 4 MPa pCO₂, with and without 4% O₂.

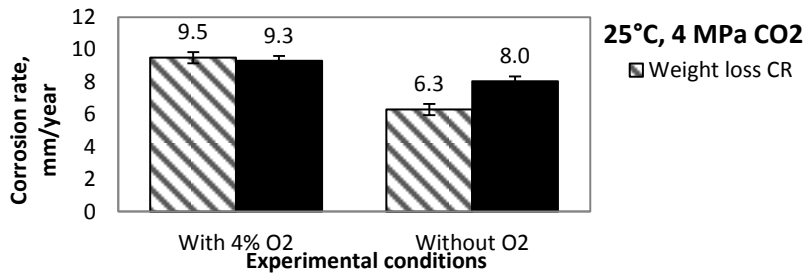


Figure 3: Weight loss corrosion rates compared to LPR time-integrated corrosion rates for experiments at 25°C, 4 MPa pCO₂, with and without 4% O₂.

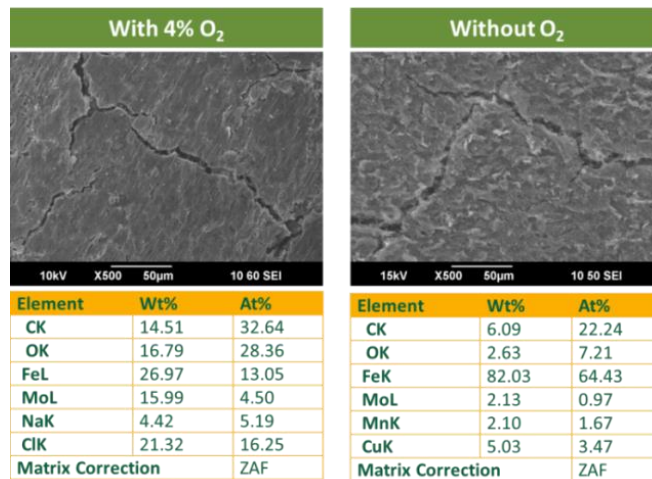


Figure 4: EDS analysis of steel surface for tests at 25°C, 4 MPa pCO₂, with and without O₂.

Cross-sectional analysis of the steel samples revealed a layer on top of the steel surface with loose and fragile microstructural features, typical of skeletal iron carbide. The thickness of the corrosion product, as seen in Figure 5, did not conform to an expected thickness of residual carbide on the steel surface. Due to its fragile nature, some amount of iron carbide was lost during the tests. The amount of iron loss in the O₂ experiment, based on the weight loss corrosion rate, corresponds to an approximate 52 μm thickness, as compared to the 15 μm thick layer of carbide/alloying element residue observed under SEM. XRD analysis, shown in Figure 6, confirmed the presence of this iron carbide layer. Removal of the corrosion product layer revealed uniform corrosion; no pits were observed on the bare steel surface.

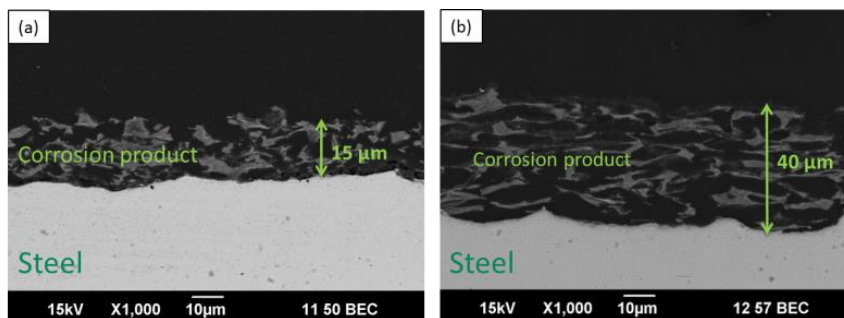


Figure 5: Steel cross-sections for tests at 25°C, 4 MPa pCO₂, (a) with O₂, and (b) without O₂.

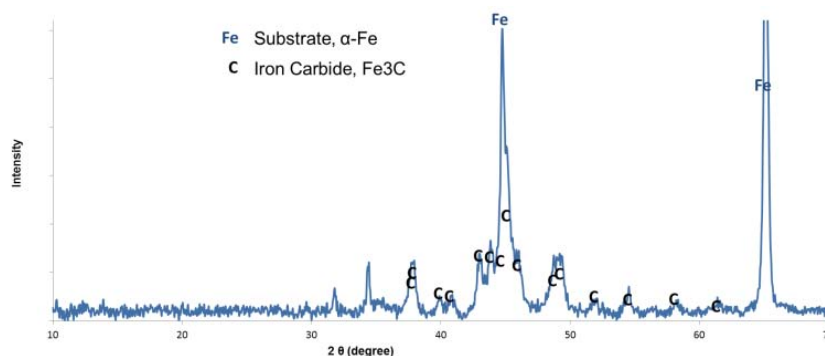


Figure 6: XRD analysis for specimen at the end of 25°C, 4 MPa pCO₂, with 4% O₂ experiment.

Experiment 2: 25°C, 9 MPa pCO₂, with and without 4% O₂.

At this condition, CO₂ is compressed into a liquid phase. The corrosion rates, measured by LPR, showed a similar trend of higher corrosion rates of steel observed in the presence of O₂, as shown in Figure 7. The presence of O₂ did not significantly affect the corrosion potential. The weight loss corrosion rate is higher in the presence of O₂ as shown in Figure 8.

The appearance of each steel surface at the end of the experiments was similar to that observed at 4 MPa CO₂. Neither obvious crystalline features nor precipitate accumulation were found, as can be seen in Figure 9. EDS indicated that O was more abundant as compared to the experiment conducted in the absence of O₂. Alloying elements such as Cu, Mo, and Ni were detected on the steel surface. The cross-sectional view of the specimens showed typical features of loose iron carbide layers on the steel surface, as shown in Figure 10. The presence of this iron carbide layer was again confirmed by XRD analysis (Figure 11). Corrosion product removal treatment was applied on the steel, revealing uniform corrosion and no obvious pits were found on the bare steel surface.

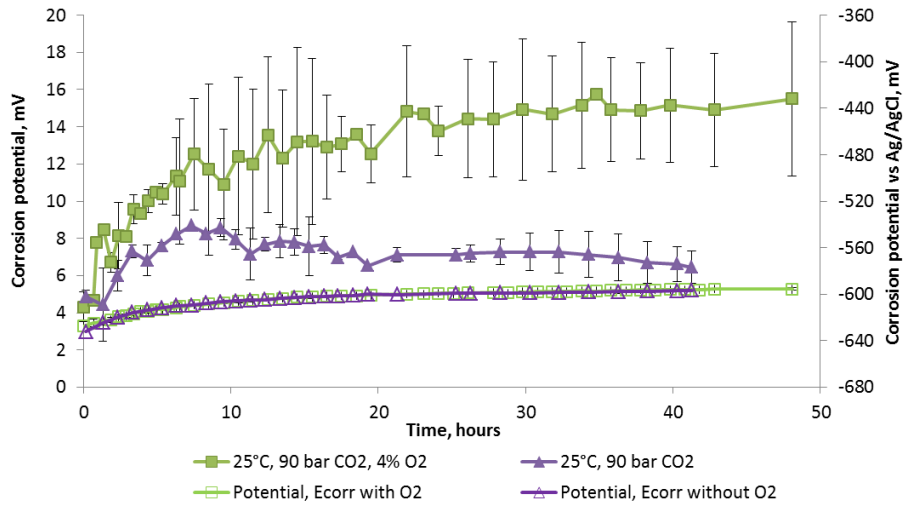


Figure 7: LPR corrosion rate and its corresponding corrosion potentials with time for experiments at 25°C, 9 MPa pCO₂, with and without 4% O₂.

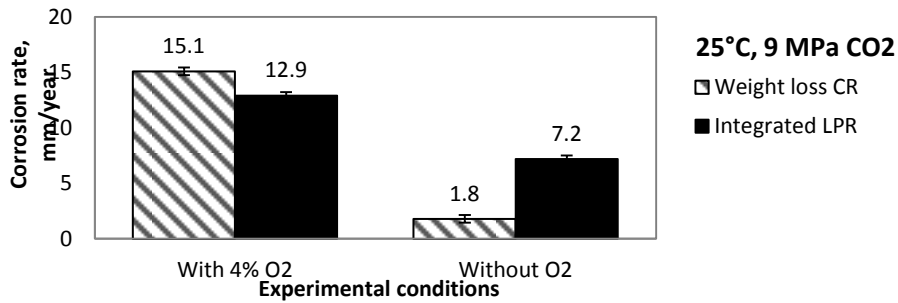


Figure 8: Weight loss corrosion rates compared to LPR time-integrated corrosion rates for experiments at 25°C, 9 MPa pCO₂, with and without 4% O₂.

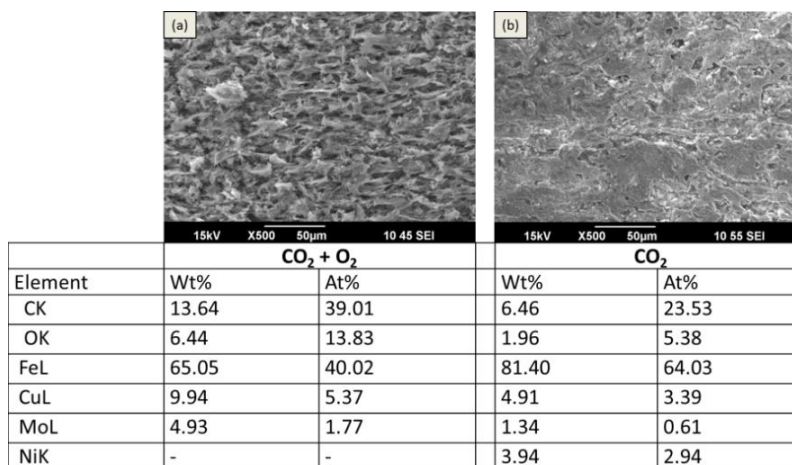


Figure 9: SEM and EDS analysis of steel surface for tests at 25°C, 9 MPa pCO₂, (a) with 4% O₂ and (b) without O₂.

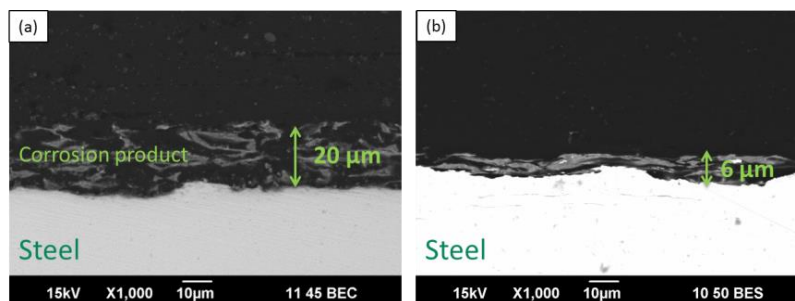


Figure 10: Steel cross-sections for tests conditions at 25°C, 9 MPa pCO₂, (a) with 4% O₂ and (b) without O₂.

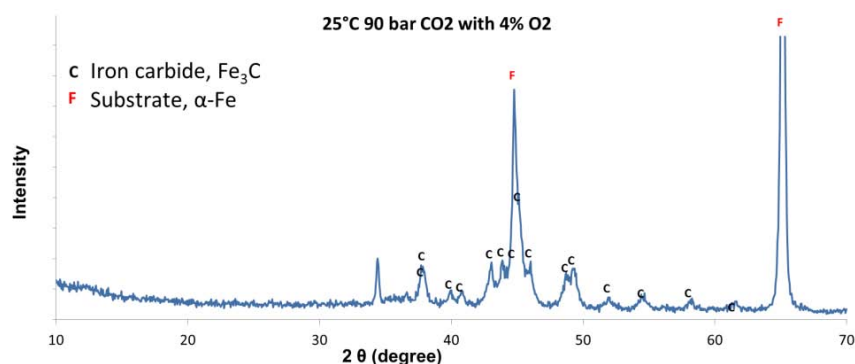


Figure 11: XRD analysis for specimen at the end of 25°C, 9 MPa CO₂, with 4% O₂ experiment.

Experiment 3: 80°C, 4 MPa pCO₂, 4% O₂.

In this experiment, the CO₂ is in the gaseous phase. Electrochemical measurements using LPR, shown in Figure 12, indicated changes of the corrosion rate throughout the duration of the experiment for both conditions, i.e. with and without O₂. Both conditions showed high corrosion rate during the first few hours of the experiment which then dropped to values less than 0.5 mm/year. Corrosion rates with O₂ ingress reached a maximum of about 47 mm/year as compared to 18 mm/year for baseline CO₂ corrosion. O₂ ingress exhibited higher final LPR corrosion rate (0.7 mm/year) than the baseline condition (0.1 mm/year). The plots using the open squares and diamonds in Figure 12 represent the corrosion potential that was measured throughout the duration of each experiment. Both systems exhibited a steady increase in potential due to the formation of protective layers on the steel surface from 10 hours to 20 hours, concurrent with the decrease in corrosion rate. The slow increase in the corrosion potential (about 150 mV) until 40 hours, as seen in the baseline experiment, then became relatively constant at around -440 mV. This may be due to the development of a corrosion product layer that provided protection to the steel surface. The presence of O₂ resulted in a sharp increase (about 400 mV) in the corrosion potential which later dropped after 20 hours and then became constant at about -420 mV around 40 hours. Based on the potential change, the formation of a corrosion product layer with the presence of O₂ is more rapid due to the increase in oxidizer concentration in the system.

Corrosion rate was also measured by weight loss method, which was then compared with the integrated values of corrosion rates from the LPR measurements. The weight loss method represented the value of the overall corrosion rate during the 48-hour period whereas the LPR corrosion rates were measured continuously throughout the test duration. The comparison, which can be seen in Figure 13, showed that the weight loss corrosion rates were comparable with the LPR corrosion rates. The presence of O₂ in this experiment resulted in a higher corrosion rate.

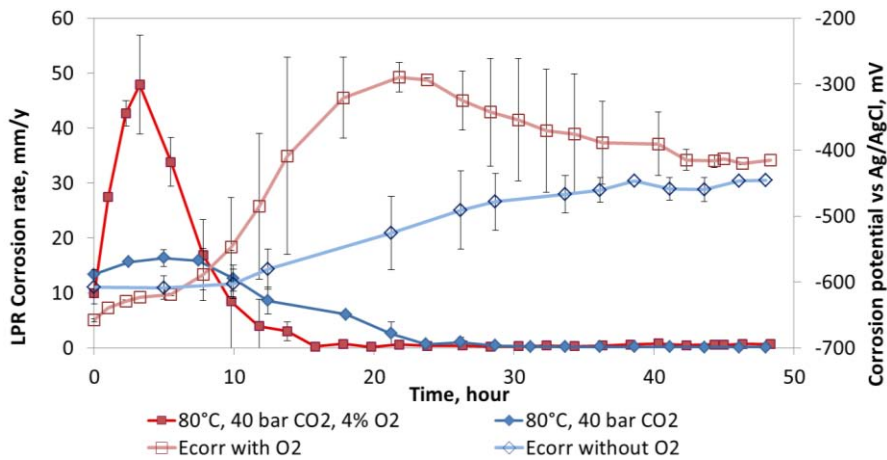


Figure 12: Comparison of corrosion rates and its corresponding corrosion potentials of steel at 80°C and 4 MPa CO₂ with and without O₂.

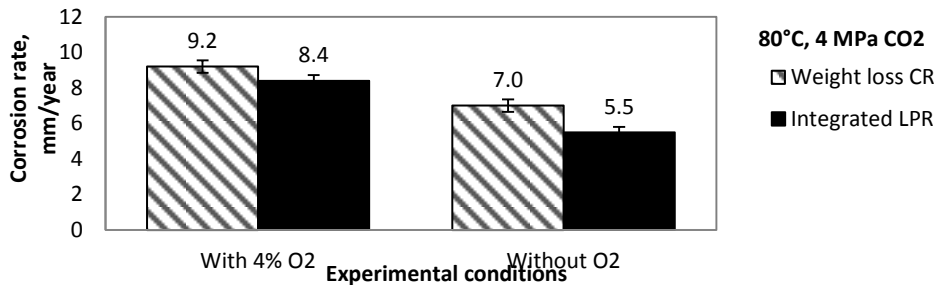


Figure 13: Corrosion rates measured using weight loss technique compared with integrated LPR results for conditions with and without O₂ at 80°C, 4 MPa CO₂ after 48 hours.

At the end of the experiment, the steel specimens, exposed to the condition with O₂, were covered with loose red products that were easily dislodged when rinsed with isopropyl alcohol. This is a preliminary indication that iron oxides were produced during the test. The reddish layer was loose, porous, and prone to dislodge, exposing the grayish inner corrosion product layer. Further observations of the specimen surface using scanning electron microscopy (SEM) revealed two different kinds of crystal morphologies (Figure 14). The non-adherent top layer consists of globular crystals that are typical of iron oxides while the features underneath the top layer were a layer of prism-like crystals which are characteristic of FeCO₃.

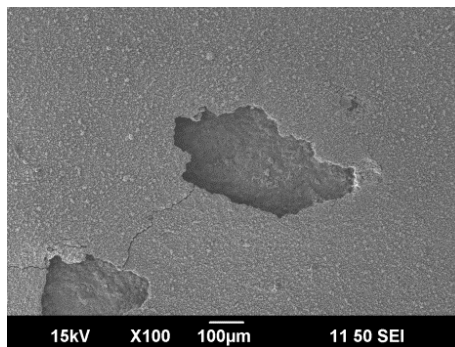


Figure 14: Steel surface after being exposed to 80°C, 4 MPa CO₂, 4% O₂ in solution for 48 hours.

The thickness and compositional characteristics of the corrosion product were determined by preparing a cross-section of the specimen which was then analyzed under SEM using backscattered electrons, as shown in Figure 15. The thickness of the corrosion product that was exposed to the CO₂/O₂ environment was relatively thinner (43 μm) than the corrosion product that was not subjected to O₂ (78 μm). The backscatter image in Figure 15(a) suggests different compositions and layers of the corrosion product based on the different shades of gray. The lighter shade of gray at the top layer indicates a heavier compound than the layer next to the steel surface. This is a good indication that the top layer consists of oxides, Fe_xO_y, while the layer closest to the steel surface is iron carbonate, FeCO₃. The nature of the bottom-most layer was observed to be more coherent and compact than the top-most layer, providing a good protection to the steel surface.

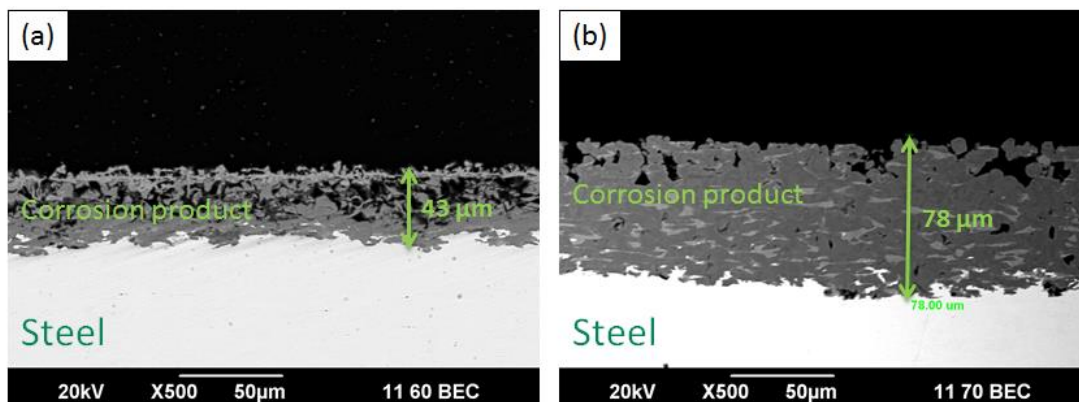


Figure 15: Cross-sectional view of steel specimen for tests conditions at (a) 80°C, 4 MPa pCO₂, 4 % O₂ and (b) 80°C, 4 MPa pCO₂.

Further investigations were carried out to observe the surface profile of the steel underneath the corrosion product after exposure to experimental conditions with O₂ present. After carefully removing the corrosion product, the bare steel surface was analyzed using optical 3D profilometry. Localized corrosion was observed on the bare steel surface and the surface profile, Figure 16, showed a pit depth up to 386 μm. This maximum pit depth value converts to about 70 mm/year of penetration rate.

Localized corrosion was quantified by calculating the pitting ratio (PR) using the following method¹¹:

$$PR = \frac{\text{Pit penetration rate}}{\text{Weight loss corrosion rate}} = \frac{70}{9.2} = 7.6$$

According to the common definition, if the PR value is greater than 5, it is a sign of localized corrosion. If the PR value is lower than 3 this suggests general roughening and no localized corrosion.¹¹ In this case, the PR value indicates the existence of localized corrosion.

X-ray diffraction (XRD) was utilized to determine the type of corrosion product that was formed on the steel surface. The diffraction pattern in Figure 17 indicated intense peaks of FeCO₃, which confirmed the coherent layer of compact corrosion product that was observed in the backscatter micrograph in Figure 15(a). Iron oxides and hydroxide were also detected on the steel surface. However, the intensities of magnetite and hematite peaks were low and difficult to distinguish between one another. Raman spectroscopy was later utilized to investigate the corrosion product crystals. The reddish-colored top layer gave spectra that are characteristic of hematite (Fe₂O₃), while the gray-colored layer (underneath the dislodged top layer) yielded strong peaks of iron carbonate, FeCO₃, as shown in Figure 18.

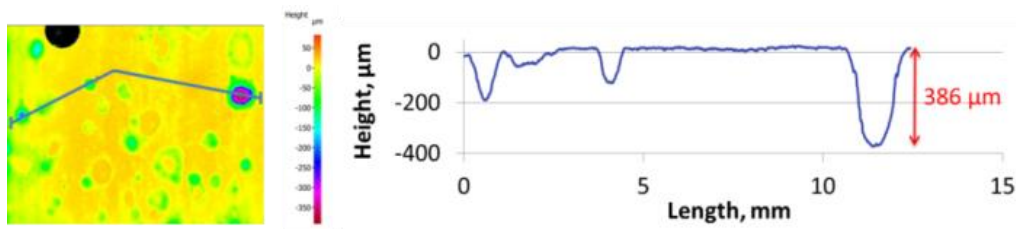


Figure 16: Surface profilometry of bare steel for test conditions 80°C, 4 MPa pCO₂, 4% O₂

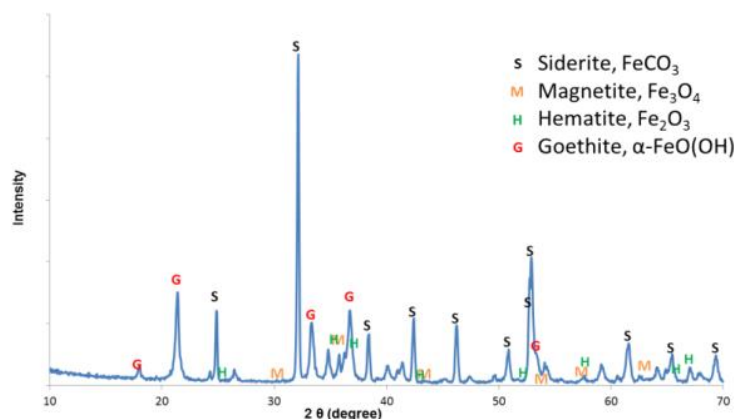


Figure 17: XRD analysis for specimen at the end of 80°C, 40 MPa pCO₂, with 4% O₂ experiment.

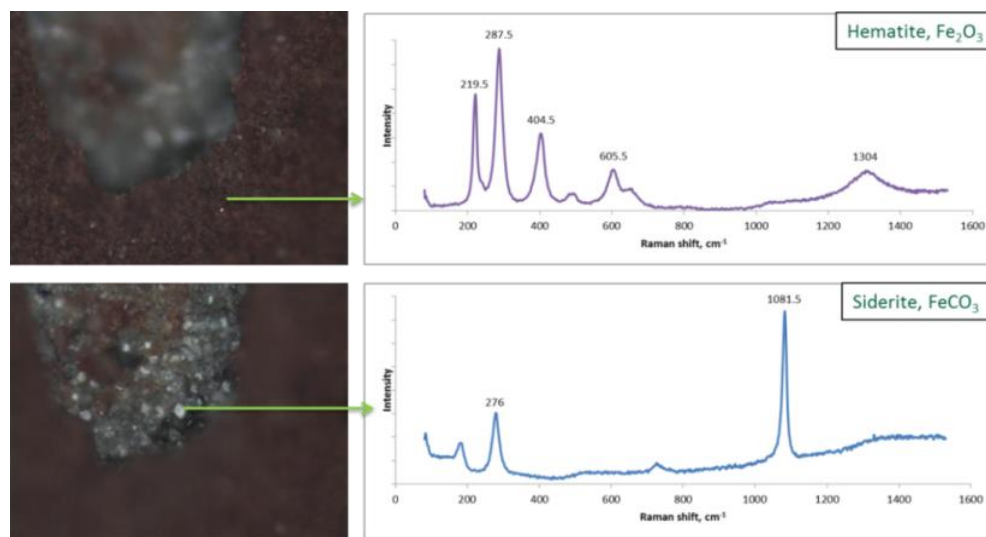


Figure 18: Raman spectra at two different locations on the steel specimen (785 nm laser excitation energy at 50 mW laser power, 20 s integration time).

To summarize the results, the presence of 4% O₂ in 4 MPa CO₂ at 80°C was detrimental to steel integrity. Even though low corrosion rate was recorded at the end of the experiment, severe localized corrosion was observed and could consequently cause failure, although the coherent and compact layer of FeCO₃ on the steel provides some protection to the steel, thus lowering the uniform corrosion rate.

Experiment 4: 80°C, 9 MPa pCO₂, 4% O₂.

In this experiment, CO₂ is in the supercritical phase. Figure 19 shows the corrosion potential and corrosion rates measured by LPR for 48 hours at 9 MPa CO₂ and 80°C. The behavior of the corrosion rates and potential at 9 MPa CO₂ showed similar behavior as the experiments done at 4 MPa CO₂ as discussed in the previous section. Higher corrosion rate was observed in the first 5 hours of experiment for the oxygenated system as compared to the anoxic system. The mean corrosion rate with O₂ ingress reached a maximum of about 36 mm/year as compared to the maximum of 26 mm/year for the baseline test. The corrosion potential showed a similar increase in its values due to the formation of a thin, relatively passive, corrosion product layer on the steel surface.

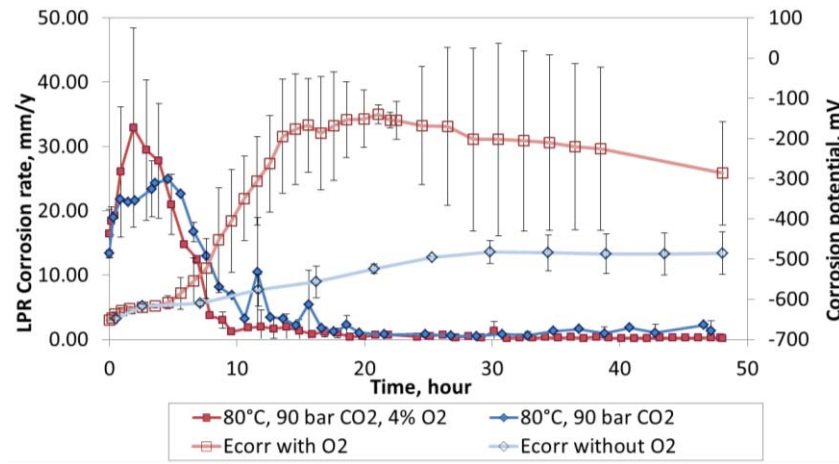


Figure 19: Comparison of corrosion rates and its corresponding corrosion potentials of steel at 80°C and 9 MPa CO₂ with and without O₂.

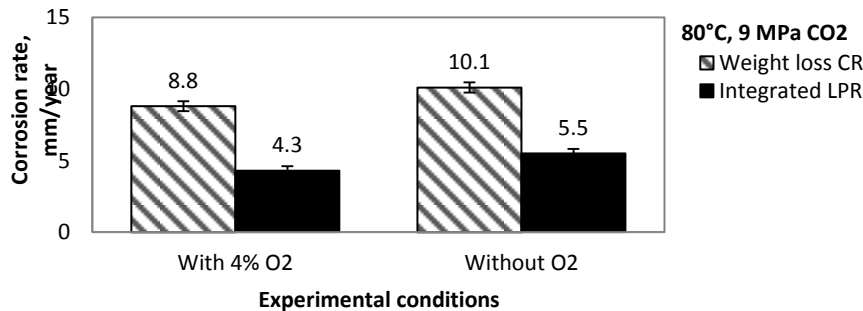


Figure 20: Corrosion rates measured using weight loss technique compared with integrated LPR results for conditions with and without O₂ at 80°C, 9 MPa CO₂ after 48 hours.

The steel specimen at this condition was covered with a thick layer of reddish precipitate that was loose and porous. Distinct layers of corrosion product were identified using backscatter SEM based on the different shades of gray on top of the steel surface shown in Figure 21. These findings were similar to those at 4 MPa CO₂ at the same temperature. The identity of the corrosion product was confirmed by XRD (Figure 22) and Raman spectroscopy (Figure 23). Due to the thickness of the top oxide layer, hematite was the only compound that was detected by Raman spectroscopy.

Features as deep as 162 μm occurred on the surface of the steel specimen as shown in Figure 24. The calculated penetration rate based on the maximum observed depth was 30 mm/year. As the weight loss corrosion rate was 8.7 mm/year, the pitting ratio was 3.4, which is considered too low to be categorized as localized corrosion.¹¹

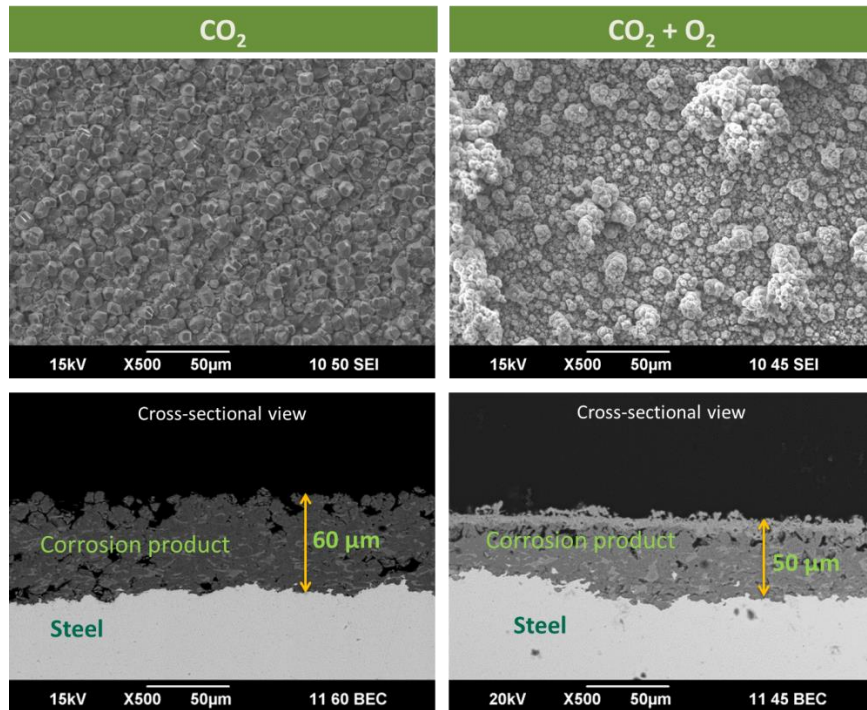


Figure 21: Micrograph of steel surface and its cross-sections comparing the effect of O₂ at 80°C, 9 MPa CO₂ in 1 wt% NaCl solution for 48 hours.

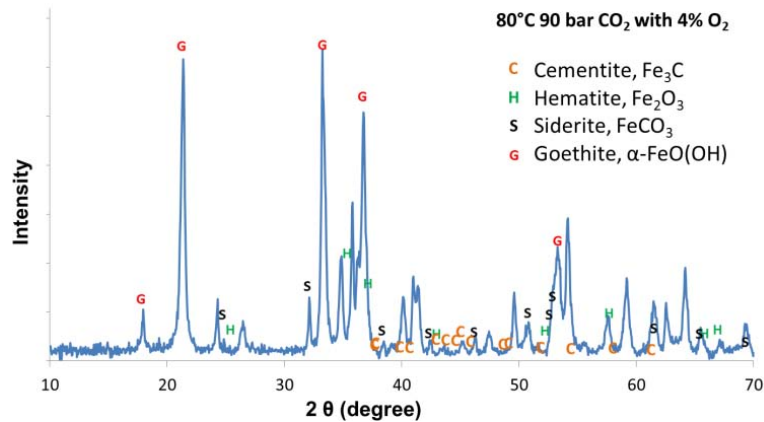


Figure 22: Analysis of steel surface using XRD for coupon at the end of 80°C, 9 MPa pCO₂, with 4% O₂ experiment.

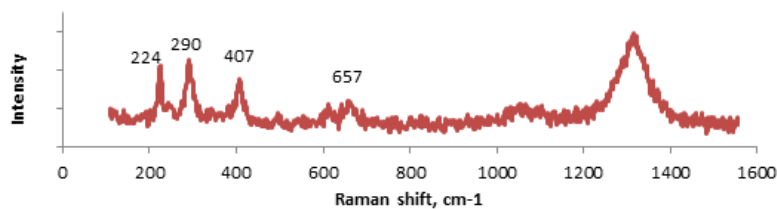


Figure 23: Hematite peaks detected using Raman spectroscopy with 532 nm laser excitation energy at 2 mW laser power, 20 s integration time.

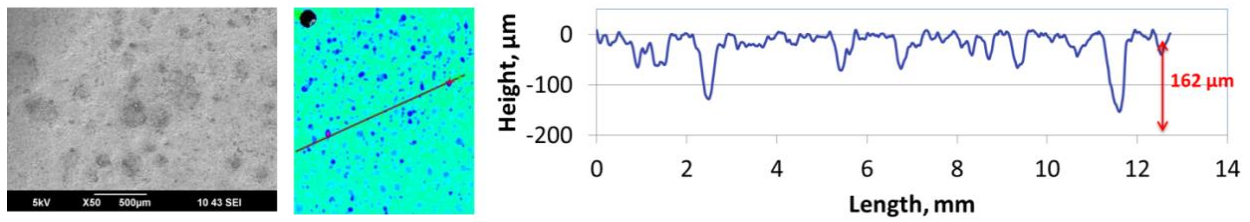
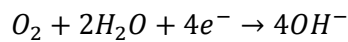


Figure 24: Surface profilometry of bare steel for test conditions 80°C, 9 MPa pCO₂, 14% O₂

Proposed Corrosion Mechanism

The ingress of O₂ causes a more complex electrochemistry compared to that of pure CO₂ corrosion. An additional cathodic reaction takes place:



This results in an increased rate of anodic reaction to provide more electrons for the extra cathodic reaction. The dissolution of iron into Fe²⁺ and Fe³⁺ ions is increased, which explains the overall higher corrosion rate.

At low temperature (25°C), the temperature is too low for FeCO₃ or Fe₂O₃ to form effectively. Therefore, neither corrosion product was observed on the steel surface. However, in the presence of O₂, goethite (α-FeO(OH)) was observed on the steel surface as the greenish layer that turned yellowish with air oxidation. Low temperature condition is the preferred environment for formation of goethite in the presence of carbonate ions.¹² The high CO₂ partial pressure in the closed system leads to the increase of hydrogen, bicarbonate, and carbonate ions in the solution. The excess hydrogen ion and bicarbonate migrates to the steel surface to act as oxidants, causing dissolution of iron as ferrous ions, Fe²⁺. As this happens, the residual iron carbide that is in the form of pearlite, as well as alloying elements, become exposed to the surface as seen in the previous SEM micrographs and EDS analyses. Figure 25 illustrates this corrosion mechanism.

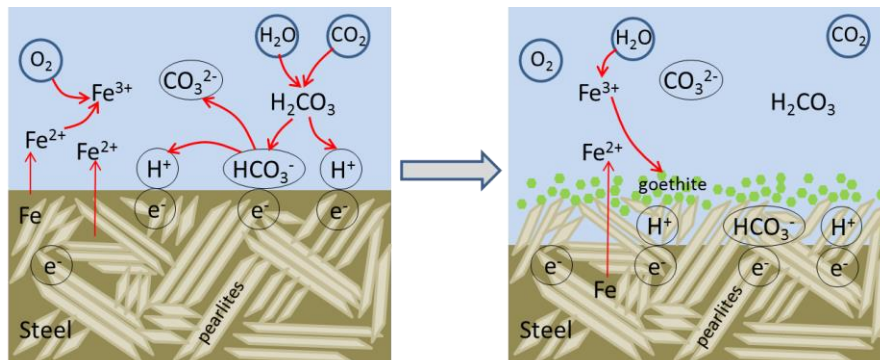


Figure 25: Proposed corrosion mechanism at low temperature and high pCO₂ with O₂ ingress in a closed system.

At high temperature (80°C), the formation of FeCO₃ and oxides are thermodynamically and kinetically favored as the precipitation rate of these species increases. The presence of O₂ interferes with the formation of FeCO₃ due to the diminished Fe²⁺ concentration in solution. The Fe²⁺ ions are oxidized to Fe³⁺ ions, which precipitate as iron oxides, and are deposited loosely and randomly on the

steel surface. The heterogeneity of the deposition provides for localized environments with the steel surface which is covered by FeCO_3 is protected, whereas the steel surface under the oxide is not. This may lead to formation of galvanic cells, even if the exact mechanism is not clear. It is possible that the O_2 that is trapped in the confined space gets consumed and depleted, creating a differential aeration cell, as typically seen in crevice corrosion.¹³ In that theory, the local area underneath the iron oxide layer becomes the anode while the larger surface area of the steel that is directly exposed to the aerated bulk solution becomes the cathode. Supersaturation of Fe^{2+} and CO_3^{2-} in the local environment is hypothesized to promote the formation of FeCO_3 in the pits as illustrated in Figure 26, but it appears to be less protective than the FeCO_3 formed elsewhere.

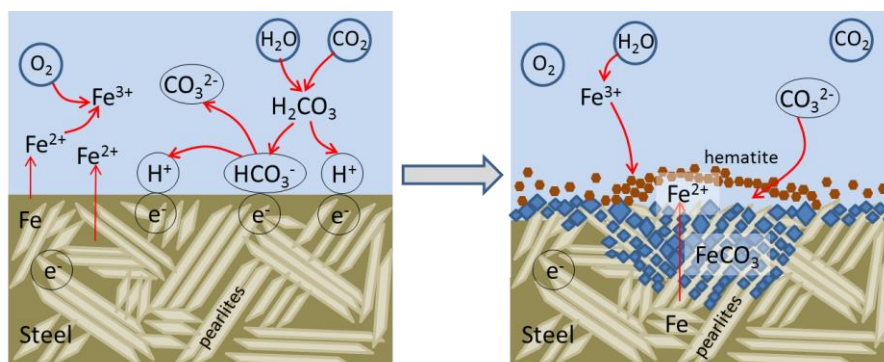


Figure 26: Proposed corrosion mechanism at high temperature and high pCO_2 with O_2 ingress in a closed system.

Further tests that are specific to studying the corrosion mechanisms under these conditions need to be conducted to confirm their validity. Investigation of galvanic cells formed at high CO_2 partial pressure might offer some answers about the mechanism of localized corrosion. Electrochemical impedance spectroscopy (EIS) may be utilized to study the corrosion mechanism at high CO_2 partial pressure in the presence of O_2 .

Summary and Conclusions

Table 2 summarizes the results drawn from the current work on the effect of O_2 in high pressure CO_2 conditions. The experiments that were conducted at 25°C caused severe uniform corrosion on specimens essentially devoid of any protective corrosion product layer on the steel surface. The final corrosion rates, measured by LPR, were considered to be high and considered unacceptable by the oil and gas industry. Tests that were conducted at 80°C revealed the formation of thick and coherent corrosion products on the steel surface that provided some defense from further active corrosion of the steel. However, localized corrosion was observed. Although the final corrosion rates were low (0.7 and 0.2 mm/year), they were still considered unacceptable for oil and gas applications where a maximum corrosion allowance of 0.1 mm/year if usually tolerated.^{14,15}

**Table 2
Results summary**

T ($^\circ\text{C}$)	pCO_2 (MPa)	pO_2 (MPa)	Final LPR corrosion rate (mm/year)	Localized corrosion?
25	4	0.17	13.6	NO
25	9	0.375	15.5	NO
80	4	0.17	0.7	YES
80	9	0.375	0.2	YES

ACKNOWLEDGMENTS

The authors would like to acknowledge the many staffs at the Institute for Corrosion and Multiphase Technology (ICMT) for their technical assistance, the Center for Electrochemical Engineering Research (CEER) for the use of XRD and Raman, the Malaysian Ministry of Education (MOE) and Universiti Teknologi MARA Malaysia for research fundings.

REFERENCES

- [1] T. Oosterkamp, J. Ramsen, "State of the art overview of CO₂ pipeline transportation with relevance to offshore pipelines," (Haugesund, Norway: Polytec, 2008).
- [2] R. L. Martin, "Corrosion consequences of oxygen entry into oilfield brines," CORROSION 2002, paper no. 02270 (Houston, TX: NACE, 2002).
- [3] J. Collier, S. Papavinasam, J. Li, C. Shi, P. Liu, J.-P. Gravel, "Effect of impurities on the corrosion performance of steels in supercritical carbon dioxide: Optimization of experimental procedure," CORROSION 2013, paper no. 2357 (Houston, TX: NACE, 2013).
- [4] Y.-S. Choi, S. Nešić, D. Young, "Effect of impurities on the corrosion behavior of CO₂ transmission pipeline steel in supercritical CO₂-water environments," *Environ. Sci. Technol.*, 44, 23 (2010), pp. 9233–9238.
- [5] Y.-S. Choi, S. Nešić, "Effect of impurities on the corrosion behavior of carbon steel in supercritical CO₂ - water environments," CORROSION 2010, paper no. 10196 (Houston, TX: NACE, 2010).
- [6] J. Zhang, X. Lin, S. Lu, T. Wang, W. Liu, S. Dong, C. Yang, M. Lu, "Corrosion behavior and mechanism of N80 steel under high temperature and high pressure CO₂-O₂ coexisting condition," CORROSION 2013, paper no. 2479 (Houston, TX: NACE, 2013).
- [7] W. Liu, S. Dong, J. Zhang, X. Lin, J. He, M. Lu, "Effect of oxygen on corrosion and erosion-corrosion behavior of N80 steel under high temperature and high pressure," presented at CORROSION 2014, paper no. 4198 (Houston, TX: NACE, 2014).
- [8] X. Lin, W. Liu, F. Wu, C. Xu, J. Dou, M. Lu, "Effect of O₂ on corrosion of 3Cr steel in high temperature and high pressure CO₂-O₂ environment," *Appl. Surf. Sci.*, 329 (2015), pp. 104–115.
- [9] N. R. Rosli, Y.-S. Choi, D. Young, "Impact of oxygen ingress in CO₂ corrosion of mild steel," presented at CORROSION 2014, paper no. C2014-4299 (Houston, TX: NACE, 2014).
- [10] C. T. Lynch, *CRC Handbook of Materials Science: Material Composites and Refractory Materials*. CRC Press, 1975.
- [11] B. Brown, "The likelihood of localized corrosion in an H₂S/CO₂ environment," presented at the CORROSION 2015, paper no. C2015-5855 (Houston, TX: NACE, 2015).
- [12] R. M. Cornell, U. Schwertmann, *The iron oxides: structure, properties, reactions, occurrences and uses*. (Weinheim: Wiley-VCH, 2003).
- [13] M. G. Fontana, N. D. Greene, *Corrosion engineering*. (New York, NY: McGraw-Hill, 1978).
- [14] A. Dugstad, L. Børvik, S. Palencsar, P. A. Eikrem, "Corrosion testing of steel armour wires in flexible pipes - a parametric study," CORROSION 2015, paper no. C2015-5829 (Houston, TX: NACE, 2015).
- [15] A. Pfennig, R. Bäßler, "Effect of CO₂ on the stability of steels with 1% and 13% Cr in saline water," *Corros. Sci.*, 51, 4 (2009) pp. 931–940.